



HAL
open science

Large scale integration of functional radio-frequency flexible MEMS under large mechanical strain

Edy Azrak, Laurent Michaud, Jérôme Richey, Alexandre Reinhardt, Samuel Tardif, Joël Eymery, Marie Bousquet, Frank Fournel, Pierre Montmeat

► To cite this version:

Edy Azrak, Laurent Michaud, Jérôme Richey, Alexandre Reinhardt, Samuel Tardif, et al.. Large scale integration of functional radio-frequency flexible MEMS under large mechanical strain. *Advanced Functional Materials*, 2022, 2022, pp.2205404. 10.1002/adfm.202205404 . hal-03883016

HAL Id: hal-03883016

<https://hal.science/hal-03883016v1>

Submitted on 2 Dec 2022

HAL is a multi-disciplinary open access archive for the deposit and dissemination of scientific research documents, whether they are published or not. The documents may come from teaching and research institutions in France or abroad, or from public or private research centers.

L'archive ouverte pluridisciplinaire **HAL**, est destinée au dépôt et à la diffusion de documents scientifiques de niveau recherche, publiés ou non, émanant des établissements d'enseignement et de recherche français ou étrangers, des laboratoires publics ou privés.



Distributed under a Creative Commons Attribution 4.0 International License

Large Scale Integration of Functional Radio-Frequency Flexible MEMS under Large Mechanical Strain

Edy Azrak, Laurent Michaud, Jérôme Richy, Alexandre Reinhardt, Samuel Tardif, Joël Eymery, Marie Bousquet, Frank Fournel, and Pierre Montmeat*

A versatile industrial recipe of transferring nitride microelectronic components such as micro-electromechanical systems (MEMS) onto flexible and stretchable substrates is demonstrated. This method bypasses difficulties of temperature-related processing, and is applicable to large-scale and mass production. The technological process of fabrication is presented along with its underlying structural and radio-frequency characterizations. In particular, the Raman strain shifts of aluminum nitride (AlN) thin films are determined for uniaxial and biaxial mechanical deformations. The transferring process onto polymer is also demonstrated by an adhesive bonding of AlN-based MEMS onto a 200 mm silicon (Si) wafer. The devices microstructure is assessed using X-ray before and after transferring, as well as their electrical radio-frequency (RF) features when on Si and polymer substrates. Then, RF measurements are also performed on the transferred and flexible devices; some in their relaxed states, and others in an in situ manner under an increasing macroscopic strain. It is shown that bulk acoustic wave resonator MEMS are fully functional even under 12% uniaxial stretching of the substrate.

example, UV-emitters,^[2] detectors,^[3] field effect transistors,^[4] and diodes.^[5] Due to its remarkable chemical stability and inertness, AlN is used as a passivation layer in different applications.^[6] At nanoscale, AlN has shown a gas detection ability owing to the variation of its electrical conductance upon superficial gas adsorption.^[7] Its high thermal conductivity but low electrical conductivity allows its use as a high- k dielectric material in many devices.^[8] Wurtzite AlN is also prominent for its piezoelectric response with high acoustic wave velocity and low thermal expansion that provide tangible advantages for piezoelectric-based micromachined devices such as bulk acoustic wave (BAW) resonators^[9,10] or surface acoustic waves (SAW) resonators.^[11] It is important to mention that the crystalline quality and orientation has a major impact on AlN-based technologies, in particular low defect and dislocation densities are required to obtain high quality micro and

optoelectronic devices.^[12] However, piezoelectric features do not require an epitaxial relationship and lower cost techniques like magnetron sputtering yielding highly-oriented textures (dominant c -axis orientation) can be used as well.^[13]

The rise of mobile and internet of things applications has increased the interest in the fabrication of low-cost lightweight bendable micro-electromechanical systems (MEMS) devices. The flexibility properties are introduced in many technological domains, for instance in field-effect transistors electronics,^[14–16] lithium-ion battery,^[17] OLED-based displays,^[18] biocompatible memories,^[19] neuromorphic computing system,^[20] and bio-integrated technologies in which sensors/devices/MEMS can be exposed to rough mechanical movements and harsh chemical environments.^[21–24]


A usual approach is based on the direct synthesis of MEMS on polymer substrate. For example, polyimide (PI) substrates can be used for flexible sensors and MEMS, taking benefits from its mechanical strength and electrical insulation. Polyimide film can be freestanding or bonded to a holder substrate, for example, silicon (Si) that can be removed by dissolving an interfacial sacrificial layer such as silicon oxide (SiO₂)^[25] and Al.^[26] Another intermediate layer can be obtained by spin-coating a PDMS (polydimethylsiloxane) layer.^[27] The separation of the sensors-on-PI from the PDMS/Si substrate is done by raising the temperature to 100 °C and peeling off. Several drawbacks are related to

1. Introduction

Aluminum nitride (AlN) has numerous technological applications related to its outstanding physical and chemical intrinsic properties. For instance, its direct wide band-gap of 6.2 eV, the largest among the wide band-gap semiconductors,^[1] combined with high-CMOS compatibility have allowed constructing AlN-based optoelectronics and electronics, for

E. Azrak, L. Michaud, J. Richy, A. Reinhardt, M. Bousquet, F. Fournel, P. Montmeat
Université Grenoble Alpes
Commissariat à l'Energie Atomique
Laboratoire d'Electronique et de Technologie de l'Information
Grenoble F-38000, France
E-mail: pierre.montmeat@cea.fr

S. Tardif, J. Eymery
Université Grenoble Alpes
Commissariat à l'Energie Atomique
Institut de Recherche Interdisciplinaire de Grenoble
MEM
NRS
Grenoble F-38000, France

 The ORCID identification number(s) for the author(s) of this article can be found under <https://doi.org/10.1002/adfm.202205404>.

DOI: 10.1002/adfm.202205404

these processes, such as a wavy polymer or air bubble formation between the polymer layer and the Si substrate due to thermal annealing. The device performance in terms of materials quality can also be affected by temperature limitations for deposition or annealing steps that are specific to each polymer. Stretching or expansion can occur when using over-threshold thermal operations. Besides, the detrimental misalignments and fractures that are temperature-induced hinder lithography or other high-precision adjustments. Even if a PDMS layer is used as a carrier to transfer the MEMS onto a polyethylene-terephthalate (PET) flexible substrate,^[9] the relaxation of internal stresses is prone to lead to carpet-like rolling of the MEMS-on-polymer structure. It is noteworthy that internal stresses are not only due to polymer, but also to the MEMS components themselves, for example a free-standing Mo/AlN/Al film can also roll up.^[28] These phenomena can also lead to fractures and cracks in the active layers, which lower the performances and lower the fabrication yield. A second way to build MEMS is transfer printing.^[29]

Excimer lasers can be used for detaching the devices from their growth glass wafer onto a polymer.^[30] In fact, the beam penetrates the backside of the glass wafer, targeting a sacrificial hydrogenated amorphous Si nanolayer (e.g., tens of nm thick) located between the layers of interest (LOI, that is, component) and the glass wafer. This results in weakening of a-Si:H bonds. For 200 mm or 300 mm wafers, full-sheet laser irradiation consumes a significant amount of energy and requires a long duration to act on the entire interface. The carrier wafer should be transparent enough to transmit the beam. This limits the types of substrates that can be used.

Instead of a-Si:H, SiO₂ layers can be employed as a sacrificial layer.^[31,32] Partially etching SiO₂ located in between the Si wafer and the layers of interest weakens the adherence between them. In ref. [31], LOI are protected by a hard-baked photoresist from the partial chemical etching of native SiO₂. Afterward, a PDMS is glued on the surface of the devices and cured to enhance the adherence. The transfer is achieved by peeling off the PDMS/devices from the Si wafer. Although this method does not require lots of energy, this process flow is long (e.g., durations of photoresist etching: 3 h; and PDMS curing: 24 h). These durations are prone to be longer in case of using larger wafers, because the buried oxide (BOX) SiO₂ is less accessible for etching. In ref. [32], non-native SiO₂ layers are used. They are grown in between the Si wafer and the layers of interest by the means of photoelectrochemical oxidation. This type of oxidation at the interface requires dipping the samples in an H₂SO₄ solution for 30 min under continuous light irradiation, and an applied voltage bias. Another method removes the SiO₂ by soaking the wafer in concentrated HF for 20 min.^[33] Consequently, these methods are hardly versatile, limiting the choice of metals and semiconductors due to etching reasons. Besides, the processing temperature, in the latter one, goes up to 1000 °C, intensifying the limitations and raising the cost.

Another method consists in using various transfers associated to multiples carrier and sacrificial wafers increasing the cost and complexity of the process.^[34]

All these kinds of transfer are hardly applicable to 200 and 300 mm diameter wafer tools and less attractive industrially. Namely because of the excessive duration of the release etch step, limited active materials (e.g., using harsh acid solutions

for the release) and substrate wafers (e.g., required transparent for laser use), lower scale of the transfers (e.g., few mm² to cm² of patterns), the use of multiple temporary wafers, and lower reliability (e.g., 70% of patterns are transferred).^[29,35] As a comparison, the transfer printing proposed in this manuscript enables successful complete transfers of 200 mm wafers.

Compared to rigid devices, the performance of flexible ones might vary due to deformations, cracks, and to the influence of internal strain on AlN piezoelectric constants.^[36] The resulting non-linear AlN piezoelectric response has been studied in literature as well as the AlN band-gap,^[37,38] and the charge mobility dependence on strain.^[39]

We have previously developed an industrial process for transferring a single-crystal Si (c-Si) film or a polycrystalline AlN film from an Si substrate onto a flexible polymer.^[40–42] In this work, we carefully adjusted this process in order to transfer AlN/Si thin layers and MEMS devices on polymers using silicon-on-insulator (SOI) 200 mm wafers. This new process is detailed first, and the uni-(bi)-axial microscopic strains measured in the AlN thin-films by Raman spectroscopy under mechanical deformation are reported. With the internal reference provided by the thin Si layer sandwiched between the AlN and the polymer substrate, the effective strain applied to AlN is determined, as well as the Raman stress factor for both uniaxial and biaxial strains. X-ray diffraction is further used to characterize the crystal quality of AlN thin-films during the application of external uniaxial tensile strains. We further show that this recipe can easily be optimized for industrial processes (e.g., on 300 mm wafers) to transfer MEMS components onto polymer substrates, bypassing all the previously mentioned deleterious effects reported in literature. Finally, we report in situ X-ray diffraction and radio frequency (RF) measurements of the mechanical and electrical properties of MEMS components under uniaxial deformations.

2. Adhesive Bonding Transfer of AlN/Si Layers on Polymer

The AlN growth substrates are 200 mm silicon-on-insulator Unibond wafers, with a 205 nm-thick, [100]-oriented crystalline Si (c-Si) film on a 400 nm-thick BOX film, itself on top of a 725 μm-thick Si wafer (Figure 1a). More information about the processing machines is mentioned in Section S1-1, Supporting Information. Standard lithography, using one patterning mask, is performed to pattern the ultra-thin c-Si film to get suitable shapes for biaxial and uniaxial tensile machines, that is, disk and rectangular patterns (Figures 1b and 2a).

PVD-grade (physical vapor deposition) polycrystalline AlN (pc-AlN) films, with thicknesses between 200 nm and 1200 nm, are grown using reactive DC magnetron sputtering of a high purity Al target under Ar/N₂. The wafers are held at 350 °C, with a chamber pressure of 2.5 mTorr, and 2 kW RF power (see Figures 1c and 2b). The DC power is adjusted to maintain the residual film stress within ±100 MPa.^[43]

Wafer edges are trimmed 1.5 mm wide starting from the outer edge of the wafer, and a few hundreds of μm in depth (Figure 1d). This step ensured an optimal mechanical grinding of the Si substrate: without trimming, the wafer edges are fragile upon thinning and could fracture subsequently.

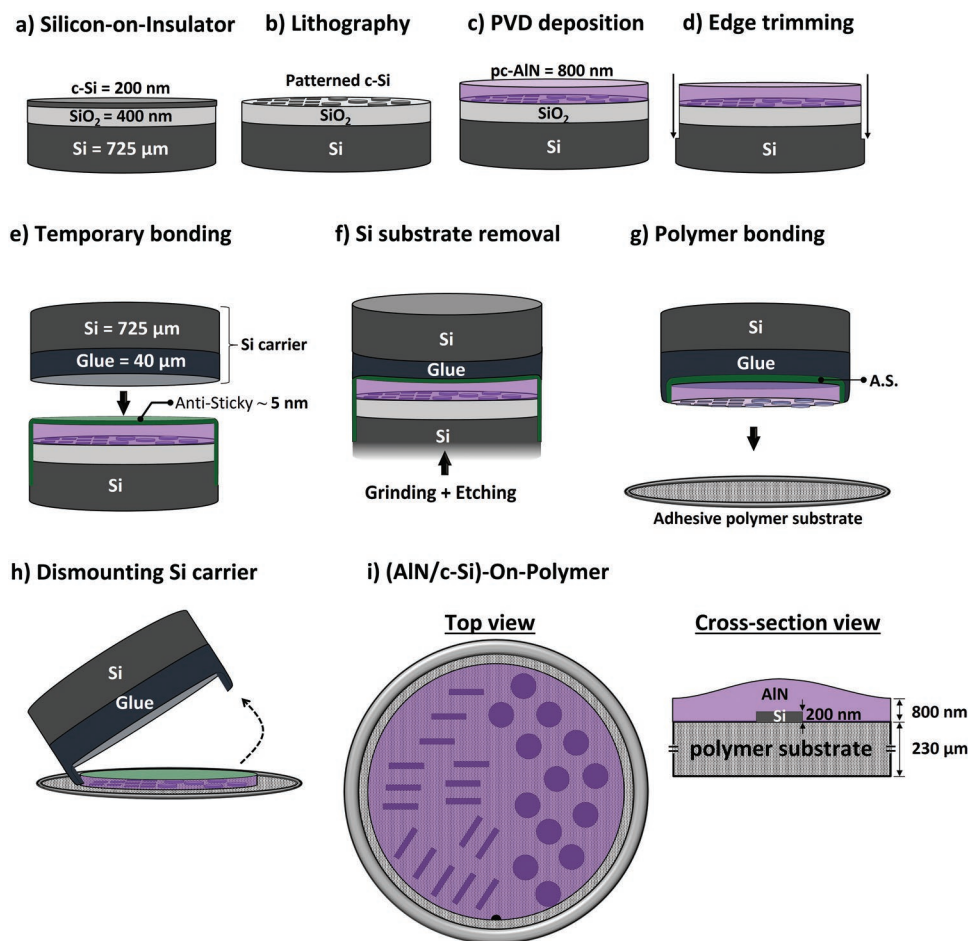


Figure 1. Schematic illustration of the fabrication of an AlN/SOI-on-polymer structure by a transfer method. a) Initial 200 mm SOI wafer constituted by 200 nm Si (100), 400 nm SiO₂ layer, and 725 μm Si substrate. b) Patterning of the c-Si thin-film using standard lithography. c) Physical vapor deposition of 800 nm AlN using magnetron sputtering on patterned Si, transparent purple is used to show the underlying Si patterns. d) Edge trimming excluding about 1 mm in diameter and a depth of few hundreds of micrometers. e) Temporary polymer bonding of the main Si substrate with a Si carrier having 40 μm of organic polymer 2 (glue). f) Grinding and chemical etching of the Si substrate. g) Polymer bonding of Si carrier onto an adhesive substrate framed on a metal-ring. h) Dismounting the Si carrier leaving the AlN/Si-on-polymer. i) Top view showing different shapes of AlN/Si samples to be used in uniaxial and biaxial strain measurements, the cross-section view shows the constitution of the AlN/Si-on-polymer: 800 nm AlN, 200 nm c-Si, on a 230 μm polymer substrate.

Afterward, an anti-sticky (NOVEC EGC-2702), abbreviated A.S., ultra-thin layer of 5 nm is spin-coated on the AlN thin-film. The A.S. reduces the adherence of the glue layer, therefore facilitating the dismantling procedure in the final step.

All polymers used from hereon are described in details in the Section SI-2, Supporting Information, and only referred to as polymer 1, 2, or 3 for the sake of clarity.

Another Si wafer called “Si carrier” with an about 40 μm-thick spin-coated organic glue (polymer 2) on its surface is used for temporary bonding at 200 °C, using an applied bonding force of 6 kN (Figure 1e). Small defects on the border may arise due to clamps, which are two metallic grips to hold the wafers during the bonding process. Photographs are added in the Section SI-3, Supporting Information to show the small untransferred region due to clamp defects on the border.

The role of the Si carrier is to hold the AlN/Si films, during the grinding and etching of the main Si substrate (Figure 1f). The main Si substrate and its BOX are removed by

a combination of mechanical grindings and chemical etching. First, a coarse thinning was performed by grinding down to 200 μm in an Okamoto tool. Afterward, fine thinning was then performed in a Disco Grinding Polishing tool to obtain the desired thickness of 50 μm (i.e., Z2 grinding wheel). The etching of the residual Si wafer is done by chemical etching (i.e., HF/HNO₃ mixture) and HF is used for removing the BOX.

The AlN/Si is then bonded on a metal-framed either adhesive polymer 1, see Figure 1g, or polymer 3 for the MEMS.

Finally, to dismantle manually the Si carrier (Figure 1h), the non-adhesive backside of the polymer is fixed on a chuck by a vacuum suction. The last step in this process, is to manually dismount upward the Si carrier, which leaves the AlN/Si films on the polymer. The A.S. layer helps in reducing the adherence between the AlN/Si and the polymer on the Si carrier. The dismantling step is achievable in industrial EVG machines, where polymer substrates are frequently used. However, before adjusting and calibrating the machines to grab the Si carrier and dismantling

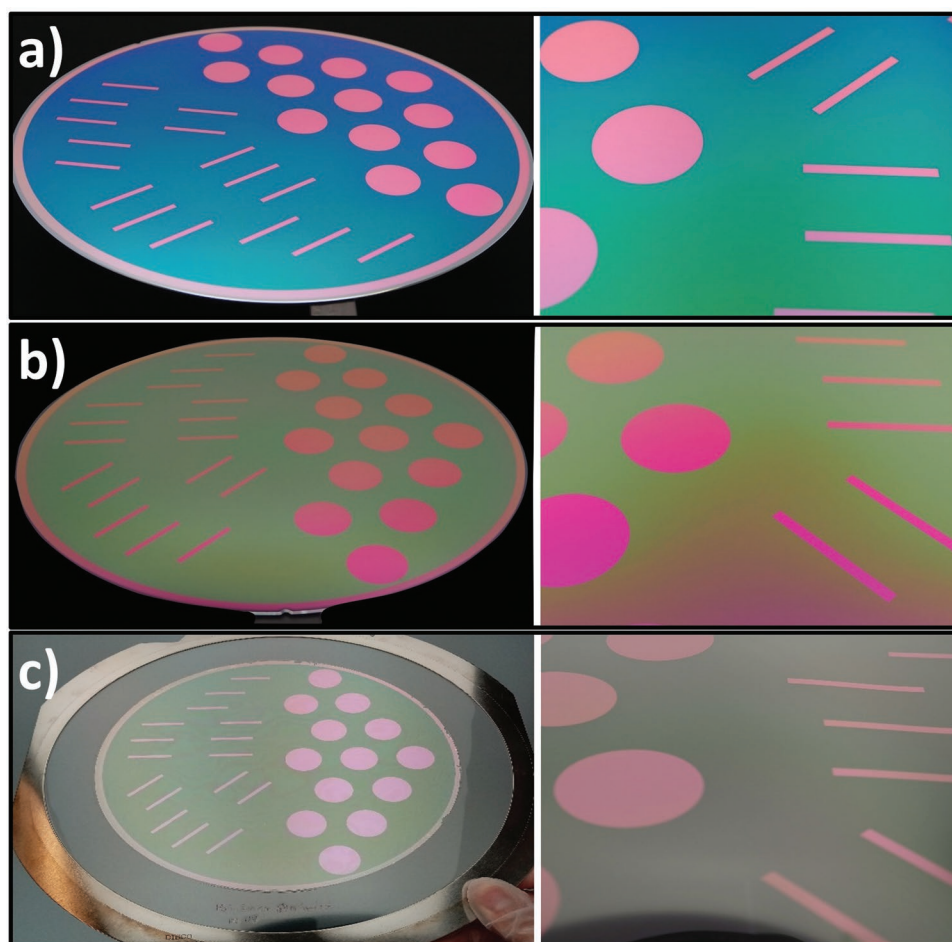


Figure 2. Photographs of the wafer a) after the patterning the 200 nm c-Si of the Unibond wafer, b) after the deposition of 800 nm thick polycrystalline AlN on the patterned crystalline Si, and c) after transferring AlN/Si to the polymer substrate. Zooms are located at the right-hand side of each picture.

it, manual handling of this process is required to prove its feasibility, as these trials are still in the proof-of-concept stage.

AlN/Si with different patterns are now located on a polymer (1 or 3) substrate, (top-view of Figures 1i and 2c). Inversely, the A.S. layer can be coated on the Si carrier (i.e., at the interface between the Si carrier and the polymer 2). Then, after completely etching the main Si substrate, AlN/Si is now located on polymer 2. Therefore, AlN/Si on polymer 2 can be easily peeled off the Si carrier. Figure 1i shows the schematics of the final stack with c-Si embedded between the AlN thin-film and the polymer substrate. The c-Si thin-film is essential, as it will be used as a strain gauge to determine the effective local strain ϵ of the AlN film. As a hypothesis, the induced-strain in c-Si is equal to that of AlN thin-film.

3. Strain Measurement of AlN/Si-on-Polymer by In Situ Raman Spectroscopy

3.1. Uniaxial-Strain

In-plane uniaxial tensile strains perpendicular to the AlN [0002] growth direction were performed on 800 nm thick AlN

covering rectangle-patterned 205 nm c-Si with [100] and [110] orientations on polymer 1. The samples have a size of $1 \times 4 \text{ cm}^2$. Experiments were performed on a HORIBA LabRAM HR Evolution Raman Spectrometer (632.81 nm laser wavelength), with a $100\times$ objective and a $1 \mu\text{m}$ diameter spot. Detailed description of AlN Raman modes, and the tensile machines were described in Section SI-3 and SI-4, Supporting Information. Samples were stretched by $1400 \mu\text{m}$ at $20 \mu\text{m s}^{-1}$ with a $50 \mu\text{m}$ elongation step. After each stretching step, the laser shutter is opened 5 s and repeated twice to improve the signal to noise ratio. The Raman peak positions were fitted by a Lorentzian curve. The c-Si signal provides an internal calibration to estimate the microscopic strain ϵ using standard Raman strain shift coefficient $\epsilon = \Delta w/b_{\text{uniax}}$, where Δw is the peak shift with respect to the unstrained Si peak and b_{uniax} is the corresponding Si-Si mode Raman strain shift. These coefficients were tabulated in literature for c-Si $\langle 110 \rangle$ and $\langle 100 \rangle$ directions: $b_{110} = -337 \text{ cm}^{-1}$, and $b_{100} = -260 \text{ cm}^{-1}$.^[41,44]

The AlN peak positions during the uniaxial strain are plotted as a function of the Si peaks for the [100] and [110] directions (Figure 3a,b). The observed linear variation allows determining the microscopic strain transferred to the AlN thin-films. Figure 3c,d shows the AlN Raman peak (E2 high-mode) shift as

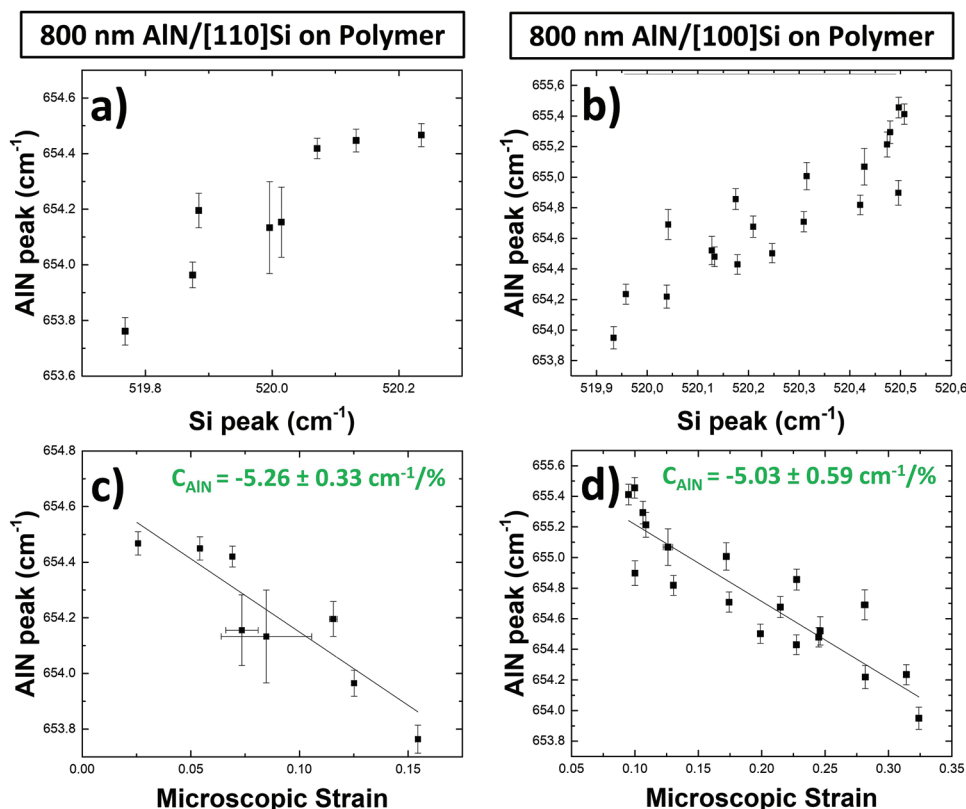


Figure 3. In situ Raman spectroscopy of uniaxially strained AlN/Si-on-polymer. Linear relationship between Raman AlN and Si Raman peaks for a) [110]-oriented Si, and b) [100]-oriented Si patterns. Peak positions of AlN grown on c) [110]- and d) [100]-oriented Si as a function of uniaxial strain. Fits of uniaxial Raman coefficients b_{110} and b_{100} are indicated in the figures.

a function of ϵ_{AlN} . The linear fittings of these data show that the Raman strain shift coefficients of the uniaxially strained AlN on [110] and [100]-oriented Si patterns are $-5.26 \pm 0.33 \text{ cm}^{-1}/\%$ and $-5.03 \pm 0.59 \text{ cm}^{-1}/\%$, respectively.

The sample elongation was measured by an optical encoder and the applied force with a force sensor. The first few elongation steps shown in **Figure 4** require a small stretching force, because the samples were curved (i.e., bowed, warped) due to the manual attachment procedure. It is noteworthy that any residual stress due to the transfer process is insufficient to cause bows or warpages of the employed samples.^[40]

The force started to increase after a few steps, and at the final stage, AlN/Si thin-films started cracking; further stretching increased the fracture sizes.

By fitting the linear stretching part of the graph for both [110]- and [100]-orientation, the spring constants (slopes) are estimated to be 7060 N m^{-1} and 6650 N m^{-1} , respectively. This behavior of the full AlN/Si-on polymer is coherent with a larger Si Young modulus along [110] (170 GPa) than along [100] (130 GPa).

3.2. Biaxial-Strain

In-plane biaxial strains perpendicular to the AlN [0002] growth direction have been also performed on circular-cut samples of AlN/Si-on-polymer for several polymer substrates polymer 1

and 2, with AlN thicknesses of 800 and 1200 nm. Three configurations are considered: 800 nm AlN on 205 nm Si located on both polymer 1 and polymer 2, and 1200 nm AlN on 205 nm-thick Si located on polymer 2. As a remark, polymer 2 is more rigid and brittle than polymer 1.

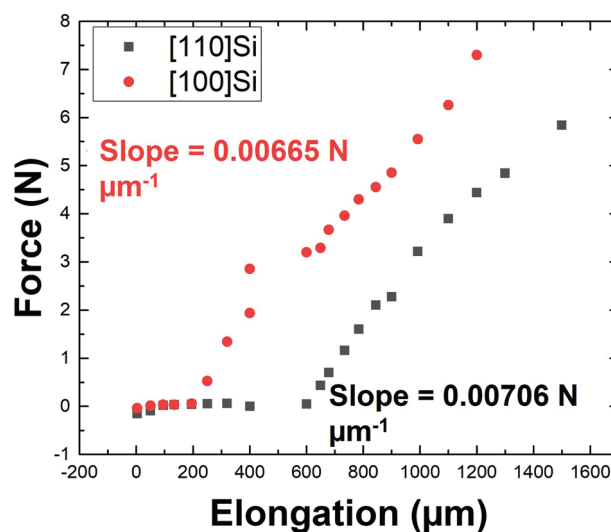


Figure 4. Force measured as a function of the applied elongation, for AlN patterns along [100]-oriented Si (red) and for AlN patterns along [110]-oriented Si (black).

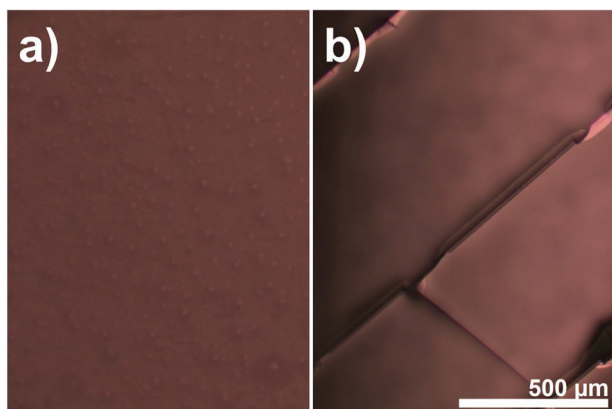


Figure 5. Optical microscope top-view images of 800 nm AlN/Si-on-polymer during bulge tensile strain tests, a) before and b) after straining (i.e., $\approx 0.24\%$ microscopic strain).

In situ Raman measurements are performed during biaxial tensile straining. The AlN/Si-on-polymer bottom interface is pressurized progressively by 0.05 bar steps, starting from $\Delta P = 0$ bar (the “relaxed” state), until the “fully strained” state is reached. After attaining the “fully-strained” state, the AlN film relaxes by cracking and the AlN Raman peak shifts back to its initial “relaxed” position.

In situ top views showing the 800 nm AlN/Si on polymer are acquired using an optical microscope during bulge tensile tests. Figure 4 shows the top surface of the attached sample prior to

tensile straining. The surface is flat with no visible fractures. Bubbles are located in the beneath polymer. Straining AlN/Si up to 0.24%, results in cracking which limits further microscopic strain. Along fracture lines, AlN/Si starts to fold forming carpet-like (e.g., rolls) structures. This is due to the manifestation of the internal strain after the local release from the polymer along fracture lines” (Figure 5).

As previously mentioned, the Si thin-film is used as an internal strain gauge, and we use $b_{\text{biax}} = 723 \text{ cm}^{-1}$ for the Raman strain shift coefficient.^[45] To confirm the linear relationship between the Si and AlN microscopic strains, the AlN peak position (E2 mode) is plotted as a function of the Si peak position in Figure 6a–c, and conversely as a function of the strain in Figure 6d–f, assuming that the in-plane strain in the Si and in the AlN are the same. The Raman strain shift coefficients deduced by linear fits are $-15.5 \pm 1.3 \text{ cm}^{-1}/\%$; $-16.08 \pm 1.16 \text{ cm}^{-1}/\%$; and $-16.03 \pm 1.13 \text{ cm}^{-1}/\%$ for the three configurations mentioned above. Considering error bars, these results show that the strain shift coefficients are neither affected by the substrate type nor by the increase in AlN targeted thickness. For the sake of comparison, taking the AlN Young’s modulus $E = 345 \text{ GPa}$, the Raman strain shift coefficients of 800 nm AlN on 205 nm Si located on both polymer 1 and polymer 2, and 1200 nm AlN on 205 nm Si located on polymer 2 are $-4.49 \pm 0.37 \text{ cm}^{-1} \text{ GPa}^{-1}$, $-4.66 \pm 0.34 \text{ cm}^{-1} \text{ GPa}^{-1}$, and $-4.64 \pm 0.33 \text{ cm}^{-1} \text{ GPa}^{-1}$, respectively. These values are close and coherent to literature results giving $-4.45 \text{ cm}^{-1} \text{ GPa}^{-1}$ although quite large discrepancies are reported (see the value of $-3.7 \text{ cm}^{-1} \text{ GPa}^{-1}$ for reference).^[36,46]

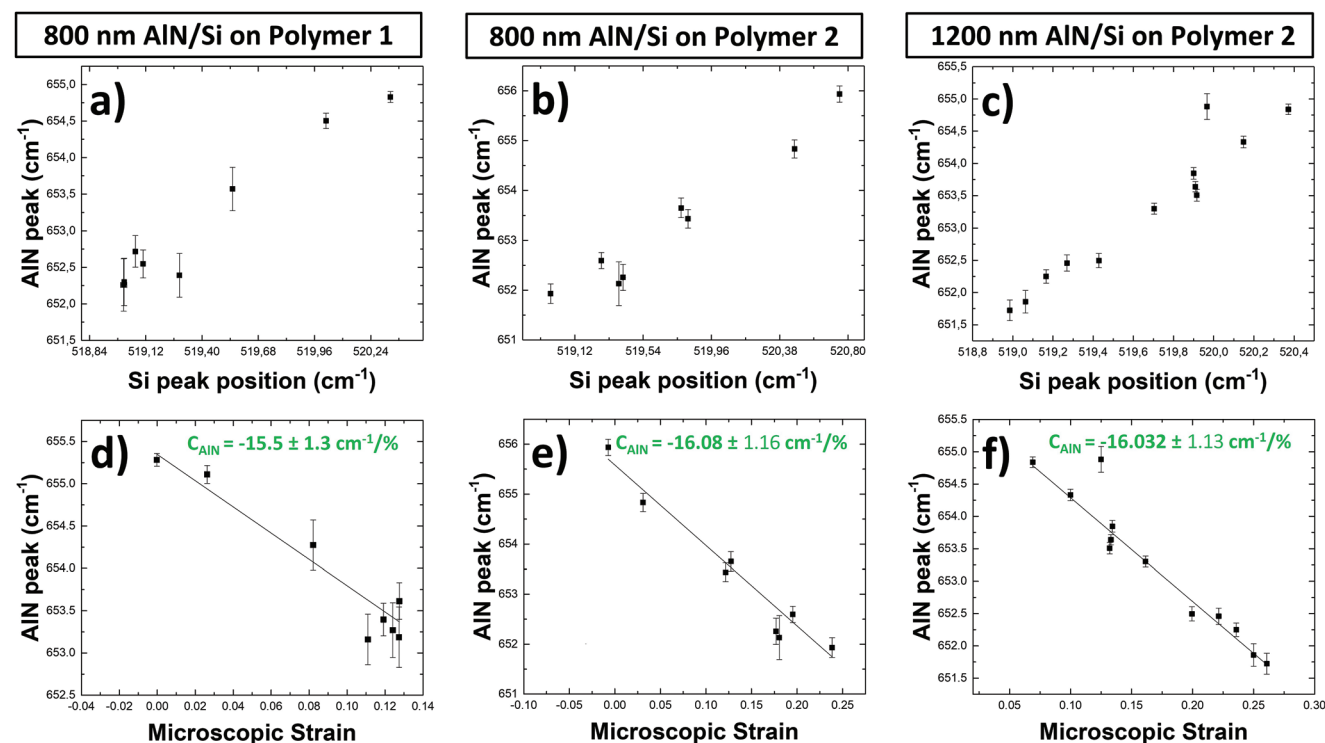


Figure 6. In situ Raman spectroscopy of biaxially strained AlN/Si-on-polymer. Linear relationship between the AlN and Si Raman peaks for a) 800 nm AlN/Si on polymer 1, b) 800 nm AlN/Si on polymer 2, and c) 1200 nm AlN/Si on polymer 2. Peak position of the AlN grown on 205 nm thick c-Si as a function of biaxial strains for d) 800 nm AlN/Si on polymer 1, e) 800 nm AlN/Si on polymer 2, and f) 1200 nm AlN/Si on polymer 2. The fitted values of the biaxial Raman coefficient b_{biax} are indicated in the figures.

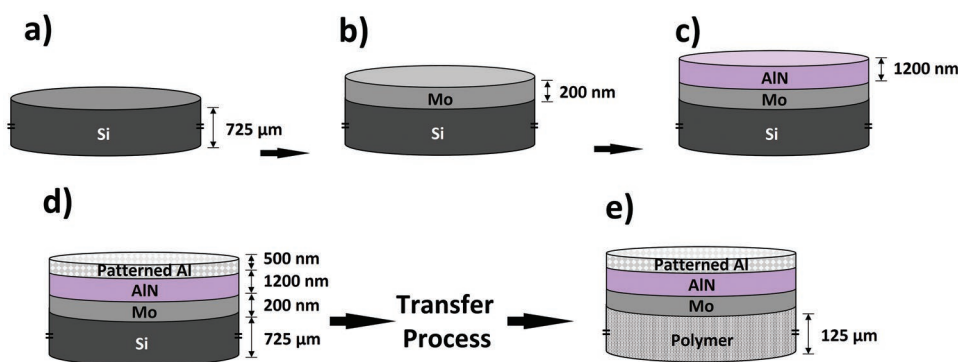


Figure 7. Schematic illustration of MEMS resonators fabrication and transfer onto polymer: a) cleaning and preparation of the 200 mm Si wafer for deposition, b) Mo deposition (200 nm) as the bottom electrode, c) AlN deposition as the active piezoelectric layer (thicknesses varying between 200 and 1200 nm), d) Al deposition (500 nm) as top electrodes, including patterning using standard lithography and wet etching, e) transfer (see text for the detailed process) onto an electronic grade polymer 2 substrate with a thickness of 125 μm.

4. Fabrication and Transfer Process of MEMS Resonators on Polymer

4.1. Process Description

MEMS, including BAW resonators, are fabricated on 200 mm Si wafer. The surface of the silicon wafer is cleaned in a CSVG wet bench, then inserted in a Sigma Fxp (Aviza Technologies) PVD magnetron sputtering cluster for subsequent deposition of 200 nm molybdenum, and 200 or 1200 nm thick [0002]-textured AlN. The two layers are deposited in sequence, without air exposure. A 500 nm aluminum top electrode is deposited using an ENDURA PVD (see Figure 7a–c). The top electrode is patterned using standard lithography followed by wet etching. The AlN piezoelectric layer and the bottom electrode underneath remain full sheet (Figure 7d). Using this particular mask, the smallest pattern is 2.5 μm (e.g., top Al electrode for SAW components).

The process previously described is used to transfer these resonators on polymers. It begins by trimming the edges of the MEMS wafer, and spin-coating an anti-sticky nanolayer on its front surface (on the top electrodes). An Si carrier with polymer 2 on its top is temporarily bonded onto the front side of the MEMS wafer. By a combination of a coarse mechanical grinding followed by chemical-mechanical etching, the primary Si substrate is totally removed, thus leaving the resonators directly bonded to the Si carrier. The exposed backside of the resonators is bonded onto the adhesive side of the polymer. Finally, the Si carrier is dismantled as shown in Figure 6e. thanks to the anti-sticky layer leaving the MEMS devices directly on polymer. Polymers 1 and 2 were used as substrates (already described above).

The optical images of the 200 mm diameter MEMS-on-Si (MOSi) wafer is shown in Figure 8a and the resulting device transfers onto a polymer substrate, that is, MEMS-on-polymer (MOP) in Figure 8b.

4.2. Microstructure Assessment of MEMS-on-Polymer Using X-Ray Diffraction

The crystal structure of the MOSi and MOP piezoelectric films was evaluated by X-ray diffraction using a

Bruker Delta-XM diffractometer (parallel beam geometry, main Cu line $\lambda(K\alpha_1) = 1.5406 \text{ \AA}$), with a particular focus on AlN and Mo thin-films texture. Symmetric 2θ - θ scans were performed before and after the transfer on polymer. Main peaks were attributed to AlN(0002), Al(111), and Mo(110) (see Figure 8c). A nearly chromatic X-ray beam is used with no additional monochromator or $K\beta$ filter, providing a high flux at the cost of Cu $K\beta$ and W $L\alpha$ lines contamination (See Section SI-6, Supporting Information for details). Peak 2θ positions for AlN(0002) on MOSi and MOP are fitted at 36.058° and 36.052° , respectively. The [110] Mo peaks are measured at respectively 40.556° and 40.541° for MOSi and MOP. These variations in peak position are within measurement uncertainty. It indicates that the transfer contribution to the strain is limited. Indeed, during the transfer process of MEMS onto Si carriers, the polymer 2 is expected to get in a tensile state due to the relatively high bonding temperature of 200 °C and to the applied bonding force of 6 kN. After the complete etching of the main Si substrate, the polymer 2 relaxes and, therefore, compresses the structure in-plane, leading to an increase of out-of-plane interatomic distances in both Mo and AlN. This expected behavior is not observed in the symmetrical scans, which show shoulder peaks on their high angle side for both AlN and Mo, indicating an in-plane tensile strain. As the main peaks are not impacted, this strain seems non-uniform and may be located on the edge of the pattern.

Rocking curve scans were also performed around the 0002 AlN diffraction peaks, as shown in Figure 8d. As expected, the AlN film shows a preferential texture along the (0002) direction, with a FWHM of 1.34° for MOSi. After transfer, a slight FWHM increase is visible with a FWHM of 1.43° , along with a high bottom baseline and a peak base broadening. The higher baseline level accounts for X-ray diffusion of the polymer substrate. The peak base broadening is most likely due to partially disoriented grains. This grain population may be linked to the strain observed in the symmetrical 2θ - θ scan. Most importantly, the slight broadening of the main peak indicates that the transfer has a limited impact on the grain orientation.

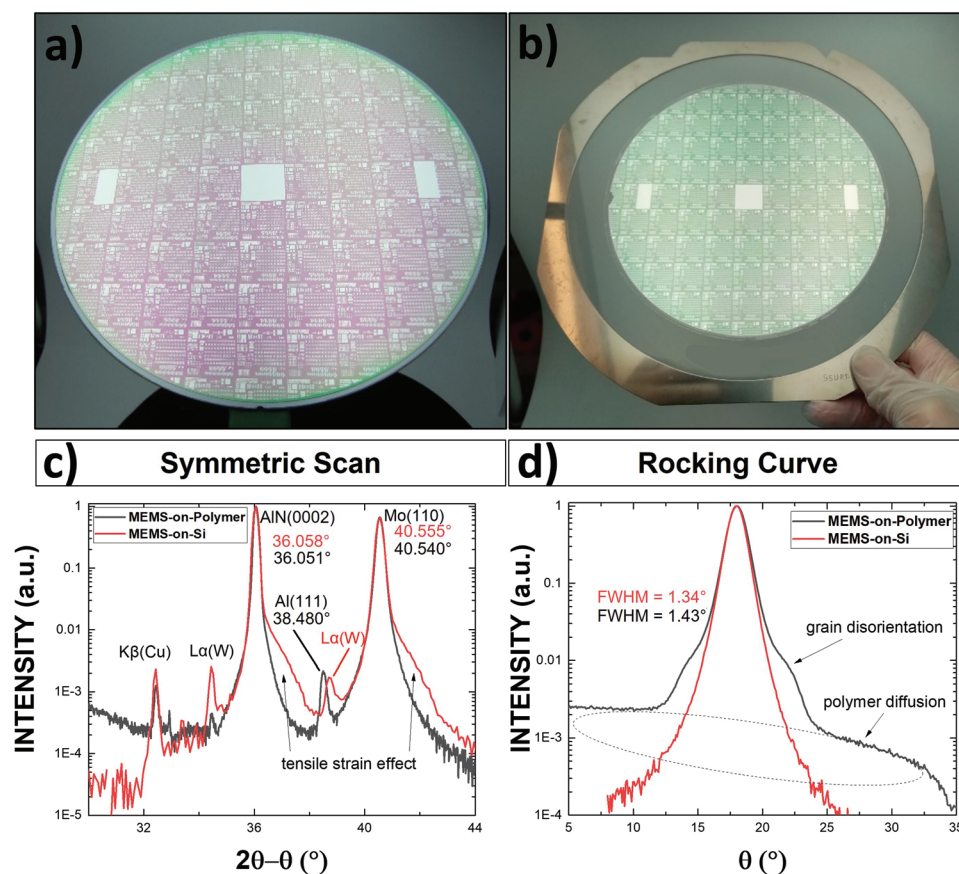


Figure 8. a) Picture of the MEMS after the deposition and patterning of the top electrode, and b) of the MEMS-on-polymer. c) 2θ - θ X-ray diffraction scan of MEMS-on-Si and on polymers, and d) rocking curve around the 0002 reflection of AlN.

5. Radio-Frequency Measurements

5.1. Ex Situ RF Measurement of Unstrained MEMS-on-Polymer and on Silicon

The electrical characterization of BAW resonators has been performed after their fabrication on Si substrate and after their transfer on a polymer film. For the purpose of device performance evaluation, no acoustic isolation was inserted between the metal/piezoelectric/metal stack and either the silicon or polymer substrate. No bottom electrode patterning has been also performed: simple resonators were defined by the circular shape of the top electrodes, surrounded by a large ground plane.^[47] Within this configuration, two resonators were measured connected in series by the full sheet bottom electrode.

For the measurements, Ground–Signal–Ground (GSG) RF probes were used to establish the electrical contact. While measurements of resonators on silicon substrates were fully standard, the measurement of BAW resonators required a careful landing of the RF probes onto the polymer: insufficient pressure prevents reaching a good electrical contact, while a too large pressure induces a large deformation of the polymer under the probes, capable of causing the AlN film to break. Hence, the positioning of the probes had to be performed manually.

The electrical scattering parameters (S-parameters) have been acquired by a network vector analyzer, sweeping the frequency from 10 MHz to 10 GHz with 500 kHz steps. These S-parameters were then directly converted to admittance before plotting in **Figure 9**.

Devices exhibit a thickness mode resonance at respectively 4.8 and 6.4 GHz for 500 and 200 nm-thick AlN films. We first fitted the measurements with a Butterworth–Van Dyke equivalent model,^[48] that is, a series RLC circuit with a parallel capacitance and a series resistance and inductance to account for ohmic losses in the electrodes, to evaluate their quality and electromechanical coupling factors. When resonators are measured on silicon substrates, their quality factors are determined respectively as 8 ± 1 for 200 and 500 nm-thick AlN films and their electromechanical coupling factors respectively $6.2 \pm 0.2\%$ and $4.2 \pm 0.2\%$. The evaluated quality factors are significantly lower than state of the art BAW resonators. This is in fact due to radiation of the acoustic waves excited in the piezoelectric film into the substrate. After transfer onto a polymer substrate, the resonances are maintained at the same frequencies and their quality factor are even improved toward 30 ± 1 , as the low density of the polymer film leads to a significant reflection of the acoustic waves at the Mo/polymer interface, hence a better confinement of waves inside the resonator. On their side, the electromechanical coupling factors are now $6.7 \pm 0.2\%$ and $3.9 \pm 0.2\%$, close to those reported on silicon.

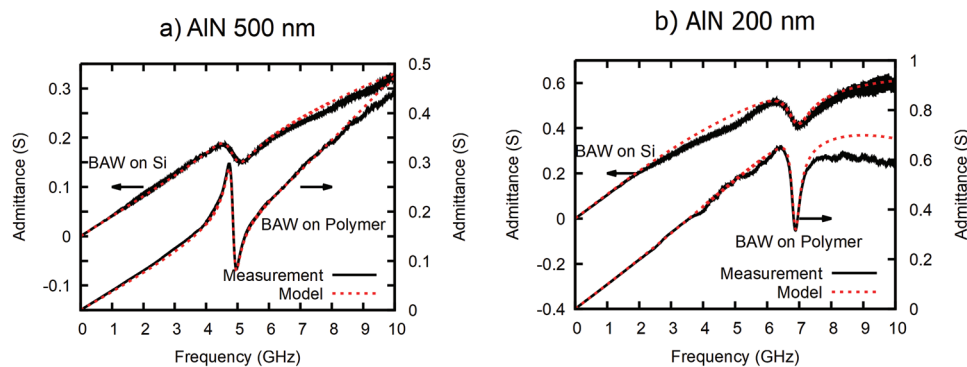


Figure 9. Radiofrequency measurements of MEMS on polymer in their relaxed state and on silicon substrate. The admittance versus electrical signal frequency of a) 500 nm AlN-based MEMS shows a resonance frequency of 4.8 GHz for both devices. b) 200 nm AlN-based MEMS shows a resonance frequency of 6.4 GHz for both devices. Dotted lines correspond to simulated responses calculated using Mason's model.^[50]

To relate the estimated electromechanical coupling factors to the piezoelectric properties of the AlN films, independently of layer thicknesses and electrical extrinsic contributions, we also fitted the electrical response with a Mason's model.^[49] This model describes the 1D propagation of acoustic waves by representing each layer in a resonator as an equivalent transmission line parameterized by its acoustic velocity, its acoustic impedance, and its thickness. The 1D assumption is valid in our case since the measured resonators are designed with radii ranging from 60 to 100 μm , that is, at least two orders of magnitude larger than Mo and AlN layer thicknesses, so that we can consider them of nearly infinite lateral extent. In the model, the polymer film is supposed semi-infinite both due to its large thickness compared to the other layers and due to its probably large acoustic attenuation. This latter assumption is further comforted by the fact that the measurements of polymer in Figure 9 are very clean and do not exhibit the noise-like contributions visible on the measurements of the same BAW resonators on Si. Indeed, these additional contributions are in fact thickness mode resonances of the silicon substrate, which acts as a thick resonance cavity and promotes therefore a large number of resonances regularly spaced by a few MHz only. However, since the Si substrate is only single side polished, the acoustic waves are scattered and do therefore not exhibit sharp resonances. For this reason, we also considered the Si substrates as infinite in the model. Eventually, we considered the material constants for Mo, AlN, and Si listed in Section SI-7, Supporting Information that we determined in previous works.^[50] On the other hand, without any knowledge of the elastic parameters of the polymer, we determined its acoustic impedance by fitting the electric response of the BAW on polymer devices. Since this parameter controls the acoustic reflection coefficient at the interface between Mo and Polymer, we could unambiguously determine it by using it to match the quality factor of the modelled response to the one of the measurements. Eventually, the resonance frequencies of the resonators were finely matched to the measurements by setting the AlN thickness to respectively 492 and 185 nm instead of respectively 500 and 200 nm. As these thickness variations remain within usual on-wafer and wafer-to-wafer thickness dispersions, no adjustment of acoustic velocities had to be introduced. Noticeably also, the spacing between the resonance

(maximum of the admittance) and antiresonance (minimum of the admittance) was directly well estimated by the thickness-adjusted model, so no change in the piezoelectric properties of the AlN film (namely, its electromechanical coupling factor) needs to be introduced to reproduce the electric response of the resonators on polymer films, whatever the thickness of AlN. This shows that the film transfer process had no significant impact on the resonators.

5.2. In Situ RF Measurement of MEMS-on-Polymer under Uniaxial Deformation

In situ RF measurements are performed on rectangular ($1 \times 4 \text{ cm}^2$) MEMS on polymer samples under uniaxial tensile strain (see Figure 10a). Similar BAWs to the ones already studied (see the left-side inset of Figure 10b) are used for in situ RF measurements except that the thickness of the active layer and the top electrode were respectively 1.2 and 0.5 μm . The device is less prone to fractures. The samples are stretched by the tensile machine in an arbitrary direction. Then, probes were landed on the top electrodes of BAW components and RF measurements were executed after each straining step. At the end of the stretching (see Figure 10b), samples are plastically deformed. Resonator responses are studied for different macroscopic strains (see Figure 10c). Three orders of resonance are measured around 2, 4, and 7 GHz, and the fundamental resonance exhibits the largest electromechanical coupling factor ($5.2 \pm 0.2\%$) and quality factors similar to the ones previously reported for devices on polymer (30 ± 1). A closer insight on the fundamental resonance at each macroscopic strain is shown in Figure 10d. Remarkably, the devices remain functional even after stretching the substrate up to 12% and the resonance peak position does not exhibit any frequency shift. This indicates that the macroscopic strain has no detrimental behavior on the RF features of the active layer, and has only a weak effect on the resonance amplitude, although mechanical plasticity of the substrate is observed at high deformation rate. We note that most of the macroscopic strain should be taken up by the most ductile sample areas, for example, outside of the devices, which are stiffer due to the additional materials layers.

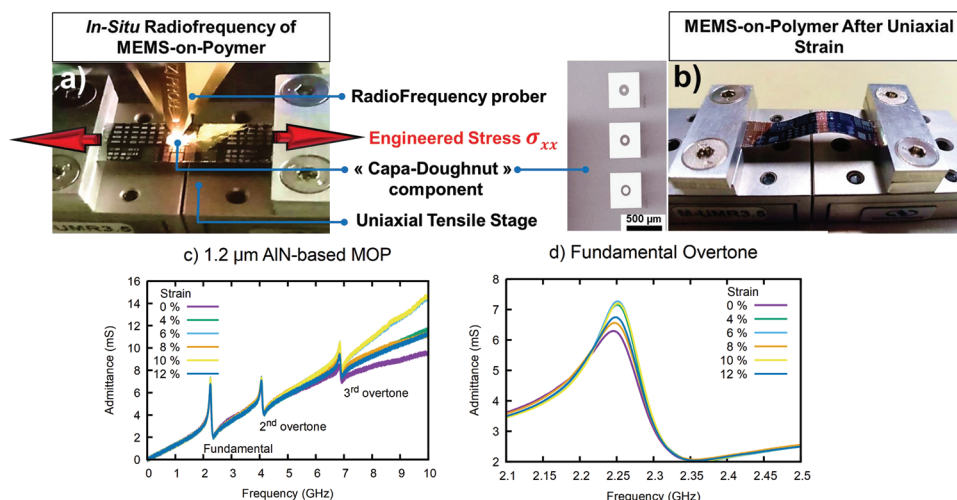


Figure 10. In situ radiofrequency measurements of BAW MEMS-on-polymer under engineered uniaxial straining a) RF probe measurement of a “Capa-Doughnut” component (shown on the right side as an inset) while applying an external uniaxial stress. b) Picture of the relaxed sample after about 8% macroscopic elongation. c) Admittance as a function of electrical frequency (the three harmonic frequencies are measured at 2, 4, and 7 GHz, respectively). d) Fundamental harmonic evolution under uniaxial elongation (from 0% to 12%).

6. Conclusions and Perspectives

As a conclusion, we demonstrate an optimized industrial recipe to obtain thin-films and functional MEMS devices on 200 mm diameter polymer substrates. Its versatility has been shown for the substrate point of view with the use of three kinds of commercial polymers, and with the transfer of different kinds of MEMS (i.e., bulk and surface BAW components). The fabrication steps have been studied by a series of tests and characterizations. The structural-behavior has been measured under mechanical stresses of AlN/Si thin-films on polymers using Raman spectroscopy. By employing Si thin-films in these samples as a microscopic internal strain gauge, uniaxial and biaxial Raman strain shift coefficients of AlN were determined to be $5 \text{ cm}^{-1}/\%$ and $16 \text{ cm}^{-1}/\%$, respectively. X-ray diffraction was first used to study the strain in the thin-films transferred on rigid Si and on stretchable polymer substrates. The measurements demonstrated that there is no significant deformation induced by the technological process, and only a slight increase of crystal disorientation about the 0002-axis has been observed. This is also confirmed by RF measurements of BAW resonators. Interestingly, the MEMS-on-polymers exhibit improved quality factors compared to MEMS-on-Si, with resonance frequencies remaining the same. The higher quality factor is explained by the acoustic energy confinement in the layers of the device. In fact, the acoustic energy transmitted to the polymer substrate is limited due the high acoustic impedance difference between the polymer and the MEMS, and the acoustic waves reflect back to the device layers. In situ RF measurements were finally performed on MEMS-on-polymer, under uniaxial mechanical stretching. In a remarkable way, the devices are still functional even after reaching maximum stretch of 12% of the initial substrate length. It opens the way for its use in deformable, conformable, and stretchable devices. Moreover, the proposed transferring process

is well-optimized and suited for large-scale fabrications. It opens new routes toward the mass production of flexible electronics at an industrial scale.

Supporting Information

Supporting Information is available from the Wiley Online Library or from the author.

Acknowledgements

The authors acknowledge the financial support of the “Bottom-Up Exploratory Program” of CEA, the French Alternative Energies and Atomic Energy Commission. The authors also thank Fabrice Perrin for the technical support on iCVD, Géraldine Romano, Jérôme Dechamp and Laurent Bally for the technical support on grinding and edge trimming, Riadh Kachtouly for the technical support on wet etching, Laurent Gonon and Vincent H. Mareau for their help on the Raman spectroscopy.

Conflict of Interest

The authors declare no conflict of interest.

Data Availability Statement

The data that support the findings of this study are available from the corresponding author upon reasonable request.

Keywords

aluminum nitride (AlN), micro-electromechanical systems (MEMS), polymer substrates, radio-frequency, strains

Received: May 12, 2022
Revised: November 2, 2022
Published online:

- [1] J. Li, K. B. Nam, M. L. Nakarmi, J. Y. Lin, H. X. Jiang, P. Carrier, S.-H. Wei, *Appl. Phys. Lett.* **2003**, *83*, 5163.
- [2] Y. Zhu, R. Lin, W. Zheng, J. Ran, F. Huang, *Sci. Bull.* **2020**, *65*, 827.
- [3] C. P. Laksana, M. Chen, Y. Liang, A. Tzou, H. Kao, E. S. Jeng, J. S. Chen, H. Chen, S. Jian, *IEEE Trans. Ultrason. Ferroelectr. Freq. Control* **2011**, *58*, 1688.
- [4] M. Qi, G. Li, S. Ganguly, P. Zhao, X. Yan, J. Verma, B. Song, M. Zhu, K. Nomoto, H. (Grace) Xing, D. Jena, *Appl. Phys. Lett.* **2017**, *110*, 063501.
- [5] H. Fu, I. Baranowski, X. Huang, H. Chen, Z. Lu, J. Montes, X. Zhang, Y. Zhao, *IEEE Electron Device Lett.* **2017**, *38*, 1286.
- [6] H. R. Choi, B. C. Mohanty, J. S. Kim, Y. S. Cho, *ACS Appl. Mater. Interfaces* **2010**, *2*, 2471.
- [7] J. Beheshtian, M. T. Baei, Z. Bagheri, A. A. Peyghan, *Microelectron. J.* **2012**, *43*, 452.
- [8] S. Huang, Q. Jiang, S. Yang, C. Zhou, K. J. Chen, *IEEE Electron Device Lett.* **2012**, *33*, 516.
- [9] X. Yang, J. Liang, Y. Jiang, X. Chen, H. Zhang, M. Zhang, W. Pang, *IEEE Electron Device Lett.* **2017**, *38*, 1125.
- [10] E. Iborra, M. Clement, J. Olivares, S. Gonzalez-Castilla, J. Sangrador, N. Rimmer, A. Rastogi, B. Ivira, A. Reinhardt, in *2008 IEEE Ultrasonics Symp.*, IEEE, Beijing, China **2008**, pp. 2189–2192.
- [11] M. Clement, L. Vergara, J. Sangrador, E. Iborra, A. Sanz-Hervás, *Ultrasonics* **2004**, *42*, 403.
- [12] B.-H. Hwang, C.-S. Chen, H.-Y. Lu, T.-C. Hsu, *Mater. Sci. Eng., A* **2002**, *325*, 380.
- [13] A. Ababneh, U. Schmid, J. Hernando, J. L. Sanchez-Rojas, H. Seidel, *Mater. Sci. Eng., B* **2010**, *172*, 253.
- [14] L. Ding, P. Joshi, J. Macdonald, V. Parab, S. Sambandan, *Adv. Electron. Mater.* **2021**, *7*, 2001023.
- [15] M. G. Stanford, C. Zhang, J. D. Fowlkes, A. Hoffman, I. N. Ivanov, P. D. Rack, J. M. Tour, *ACS Appl. Mater. Interfaces* **2020**, *12*, 10902.
- [16] D. Ji, L. Jiang, X. Cai, H. Dong, Q. Meng, G. Tian, D. Wu, J. Li, W. Hu, *Org. Electron.* **2013**, *14*, 2528.
- [17] Y. Zhao, J. Guo, *InfoMat* **2020**, *2*, 866.
- [18] J. H. Koo, D. C. Kim, H. J. Shim, T.-H. Kim, D.-H. Kim, *Adv. Funct. Mater.* **2018**, *28*, 1801834.
- [19] T. Jiang, X. Meng, Z. Zhou, Y. Wu, Z. Tian, Z. Liu, G. Lu, M. Eginlidil, H.-D. Yu, J. Liu, W. Huang, *Nanoscale* **2021**, *13*, 724.
- [20] S. T. Keene, P. Koupidenis, Y. van de Burgt, in *Organic Flexible Electronics*, Elsevier, Amsterdam **2021**, pp. 531–574.
- [21] J. T. Muth, D. M. Vogt, R. L. Truby, Y. Mengüç, D. B. Kolesky, R. J. Wood, J. A. Lewis, *Adv. Mater.* **2014**, *26*, 6307.
- [22] K. Song, J. H. Han, H. C. Yang, K. I. Nam, J. Lee, *Biosens. Bioelectron.* **2017**, *92*, 364.
- [23] J. Reeder, M. Kaltenbrunner, T. Ware, D. Arreaga-Salas, A. Avendano-Bolivar, T. Yokota, Y. Inoue, M. Sekino, W. Voit, T. Sekitani, T. Someya, *Adv. Mater.* **2014**, *26*, 4967.
- [24] D.-H. Kim, J. Viventi, J. J. Amsden, J. Xiao, L. Vigeland, Y.-S. Kim, J. A. Blanco, B. Panilaitis, E. S. Frechette, D. Contreras, D. L. Kaplan, F. G. Omenetto, Y. Huang, K.-C. Hwang, M. R. Zakin, B. Litt, J. A. Rogers, *Nat. Mater.* **2010**, *9*, 511.
- [25] K. Lee, A. Singh, J. He, S. Massia, B. Kim, G. Raupp, *Sens. Actuators, B* **2004**, *102*, 67.
- [26] L. Gwo-Bin, H. Fu-Chun, L. Chia-Yen, M. Jiun-Jih, *Acta Mech. Sin.* **2004**, *20*, 140.
- [27] S. Y. Xiao, L. F. Che, X. X. Li, Y. L. Wang, *Microelectron. Eng.* **2008**, *85*, 452.
- [28] J. Zhao, J. Han, Y. Xing, W. Lin, L. Yu, X. Cao, Z. Wang, X. Zhou, X. Zhang, B. Zhang, *Semicond. Sci. Technol.* **2020**, *35*, 035009.
- [29] X. Zeng, H. Jiang, *J. Microelectromech. Syst.* **2011**, *20*, 6.
- [30] H. E. Lee, S. Kim, J. Ko, H.-I. Yeom, C.-W. Byun, S. H. Lee, D. J. Joe, T.-H. Im, S.-H. K. Park, K. J. Lee, *Adv. Funct. Mater.* **2016**, *26*, 6170.
- [31] C. Dagdeviren, B. D. Yang, Y. Su, P. L. Tran, P. Joe, E. Anderson, J. Xia, V. Doraiswamy, B. Dehdashti, X. Feng, B. Lu, R. Poston, Z. Khalpey, R. Ghaffari, Y. Huang, M. J. Slepian, J. A. Rogers, *Proc. Natl. Acad. Sci. USA* **2014**, *111*, 1927.
- [32] N. K. Mahenderkar, Q. Chen, Y.-C. Liu, A. R. Duchild, S. Hofheins, E. Chason, J. A. Switzer, *Science* **2017**, *355*, 1203.
- [33] D. S. Wie, Y. Zhang, M. K. Kim, B. Kim, S. Park, Y.-J. Kim, P. P. Irazoqui, X. Zheng, B. Xu, C. H. Lee, *Proc. Natl. Acad. Sci. USA* **2018**, *115*, E7236.
- [34] W. T. Navaraj, S. Gupta, L. Lorenzelli, R. Dahiya, *Adv. Electron. Mater.* **2018**, *4*, 1700277.
- [35] C.-C. Huang, X. Zeng, H. Jiang, *J. Microelectromech. Syst.* **2012**, *21*, 749.
- [36] F. Bernardini, V. Fiorentini, D. Vanderbilt, *Phys. Rev. B* **1997**, *56*, R10024.
- [37] K. Shimada, T. Sota, K. Suzuki, H. Okumura, *Jpn. J. Appl. Phys.* **1998**, *37*, L1421.
- [38] P. Liu, A. De Sarkar, R. Ahuja, *Comput. Mater. Sci.* **2014**, *86*, 206.
- [39] C. E. Dreyer, A. Janotti, C. G. van de Walle, *Appl. Phys. Lett.* **2013**, *102*, 142105.
- [40] E. Azrak, L. G. Michaud, A. Reinhardt, S. Tardif, M. Bousquet, N. Vaxelaire, J. Eymery, F. Fournel, P. Montmeat, *ECS J. Solid State Sci. Technol.* **2021**, *10*, 064001.
- [41] L. G. Michaud, C. Castan, M. Zussy, V. H. Mareau, L. Gonon, P. Montmeat, F. Fournel, F. Rieutord, S. Tardif, *Nanotechnology* **2020**, *31*, 145302.
- [42] P. Montméat, I. De Nigris Brandolisi, S. Tardif, T. Enot, G. Enyedi, R. Kachtouli, P. Besson, F. Rieutord, F. Fournel, *ECS Trans.* **2016**, *75*, 247.
- [43] P. Ivaldi, J. Abergel, M. H. Matheny, L. G. Villanueva, R. B. Karabalin, M. L. Roukes, P. Andreucci, S. Hentz, E. Defaÿ, *J. Microelectromech. Syst.* **2011**, *21*, 085023.
- [44] I. De Wolf, H. E. Maes, *J. Appl. Phys.* **1999**, *85*, 7484.
- [45] S. Nakashima, T. Mitani, M. Ninomiya, K. Matsumoto, *J. Appl. Phys.* **2006**, *99*, 053512.
- [46] V. Luzzi, D. R. Clarke, *Appl. Phys. Lett.* **2006**, *89*, 241911.
- [47] R. Aigner, in *2008 IEEE Ultrasonics Symp.*, IEEE, Beijing, China **2008**, pp. 582–589.
- [48] J. D. Larson III, P. D. Bradley, S. Wartenberg, R. C. Ruby, in *Proc. of the 2000 IEEE Ultrasonics Symp.*, IEEE, San Juan, Puerto Rico **2000**, p. 863.
- [49] J. F. Rosenbaum, *Bulk Acoustic Wave Theory and Devices*, Artech House, Boston **1988**.
- [50] P. Emery, D. Petit, P. Ancey, A. Devos, in *2007 IEEE Ultrasonics Symp. Proc.*, IEEE, New York **2007**, p. 612.